Blading Phase-Pure Formamidinium-Alloyed Perovskites for High-Efficiency Solar Cells with Low Photovoltage Deficit and Improved Stability

Wu-Qiang Wu,* Peter N. Rudd, Qi Wang, Zhibin Yang, and Jinsong Huang*

Currently, blade-coated perovskite solar cells (PSCs) with high power conversion efficiencies (PCEs), that is, greater than 20%, normally employ methylammonium lead tri-iodide with a sub-optimal bandgap. Alloyed perovskites with formamidinium (FA) cation have narrower bandgap and thus enhance device photocurrent. However, FA-alloyed perovskites show low phase stability and high moisture sensitivity. Here, it is reported that incorporating 0.83 molar percent organic halide salts (OHs) into perovskite inks enables phase-pure, highly crystalline FA-alloyed perovskites with extraordinary optoelectronic properties. The OH molecules modulate the crystal growth, enhance the phase stability, passivate ionic defects at the surface and/or grain boundaries, and enhance the moisture stability of the perovskite film. A high efficiency of 22.0% under 1 sun illumination for blade-coated PSCs is demonstrated with an open-circuit voltage of 1.18 V, corresponding to a very small voltage deficit of 0.33 V, and significantly improved operational stability with 96% of the initial efficiency retained under one sun illumination for 500 h.

The power conversion efficiencies (PCEs) of perovskite solar cells (PSCs) are already higher than other well-established, commercial, thin-film photovoltaic technologies.[1] The most impressing task for commercializing PSC technology is to translate the high efficiency achieved in small-area devices into perovskite modules fabricated via scalable processes, such as the blade-coating and ink-jet printing.[2–4] By rational designing ink composition, the device performances of bladed PSCs are on par with spun ones, while blading can make large-area modules at unprecedented speed.[3,4] However, almost all bladed PSCs with PCEs over 20% still employed methylammonium lead iodide (MAPbI$_3$) as the light absorbing material, which

has a bandgap of 1.55 eV, too large for maximum efficiency.[4,5] By comparison, cubic-phase formamidinium lead iodide (FAPbI$_3$) has a smaller bandgap of 1.48 eV, which potentially can achieve higher device efficiency.[6,7] However, FAPbI$_3$ inherently suffers from poor phase stability at room temperature. It can easily convert from cubic perovskite phase to a thermodynamically more stable δ-phase (yellow-phase).[8] Several approaches have been reported to stabilize the photoactive black-phase of FAPbI$_3$ by effectively manipulating the material surface energy, including 2D/3D mixture engineering,[9,10] surface functionalization,[11] or compositional engineering with alloying of multiple cations or halide ions,[12,13] where all the perovskite films were made by spin-coating process. It is noted, alloying with 60% of MA did stabilize the preovskite phase, but also increased the bandgap. Producing a high-quality, phase-pure, FA-dominant perovskite film via blade-coating has not been achieved in the past, due to less controlled nucleation and/or crystal growth. Moreover, the device efficiency of bladed, triple-cation cesium formamidinium methylammonium (CsFAMA) perovskite-based PSCs is still below 20%, which is much lower than those MAPbI$_3$ PSCs with an even larger bandgap.[4,12,13]
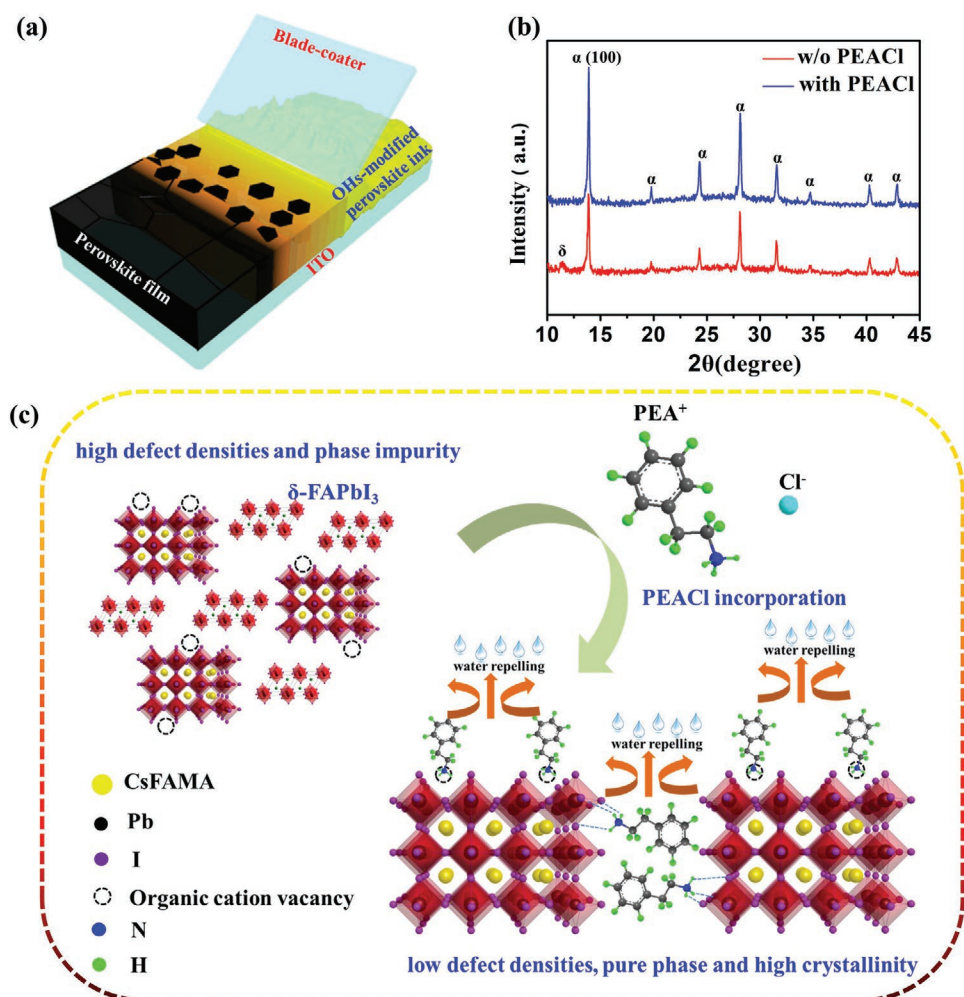
Here, we report that incorporating a small amount of organic halide (OH) molecules, namely, phenylethylammonium chloride (PEACl), in FA-alloyed perovskite thin films enhances phase purity and stability. The Cl anion could modulate the crystal growth to obtain perovskite films with high crystallinity, large grains, and low trap densities. Meanwhile, the positively charged PEA cations (PEA$^+$) passivate the charged defects at the perovskite surface and/or grain boundaries (GBs) via electrostatic interactions with A-site vacancies or forming hydrogen bonds with undercoordinated I$^-$ ions, while the hydrophobic conjugated rings are capable of enhancing the moisture resistance. PEACl addition also assists in facilitating the charge collection. As a result, we have demonstrated an optimized, phase-pure CsFAMAPbI$_3$ perovskite with a bandgap of 1.51 eV. A high PCE of 22.0% (stabilized PCE of 21.8%) has been achieved. Notably, the PSCs show a very small V_{oc} loss of 0.33 V. In addition, the ambient and operational stabilities of the devices based on PEACl-modified perovskite films have been dramatically enhanced.

Dr. W.-Q. Wu, P. N. Rudd, Dr. Q. Wang, Dr. Z. Yang, Prof. J. Huang
Department of Applied Physical Sciences
University of North Carolina
Chapel Hill, NC 27599, USA
E-mail: wuqiang.wu@uq.edu.au; jhuang@unc.edu
Dr. W.-Q. Wu
Nanomaterials Centre, School of Chemical Engineering and Australian
Institute for Bioengineering and Nanotechnology
The University of Queensland
Brisbane, QLD 4072, Australia

The ORCID identification number(s) for the author(s) of this article can be found under https://doi.org/10.1002/adma.202000995.

**ADVANCED
SCIENCE NEWS**

www.advancedsciencenews.com

**ADVANCED
MATERIALS**

www.advmat.de

Figure 1. Fabrication process, crystallographic properties, and functions of OH additives. a) Scheme showing the blade-coating process of the perovskite film. b) XRD patterns of pristine CFM and CFM modified with 0.83 mol% PEACl. c) Schematic illustration of δ-phase nonperovskite suppression, defect passivation, and water repellence induced by PEACl modification.

Figure 1a depicts the fabrication of the FA-alloyed perovskite films via a blade-coating method. In order to reduce the perovskite bandgap, it is necessary to incorporate a high ratio of FA cations in the perovskite composition. We employed a triple-cation $Cs_{0.05}FA_{0.70}MA_{0.25}PbI_3$ perovskite compound (denoted as CFM) as an initial study objective. A series of OHs featuring functionalized aromatic rings terminating with an ammonium group and various halide counterions (Cl, Br, or I) were added into perovskite inks for suppressing the formation of δ-phase nonperovskite impurities. The representative OHs were PEACl, phenylethylammonium bromide (PEABr), and phenylethylammonium iodide (PEAI). Among the various OHs, PEACl was shown to be most effective in suppressing the formation of δ-phase nonperovskite (Figure S1, Supporting Information), and the optimal additive amount was determined to be 0.83 mol% (relative to Pb) based on the intensive study of photovoltaic performances, which are summarized in Tables S1 and S2, Supporting Information. X-ray diffraction patterns (XRD) of pristine CFM and targeted CFM modified with 0.83 mol% PEACl are shown in Figure 1b. The pristine CFM perovskite film contains a notable nonperovskite δ-phase. In

contrast, adding a small amount of PEACl has effectively suppressed the formation of δ-phase and improved the crystallinity of the black-phase perovskite, as is evidenced by reduced full width half maximum (i.e., 0.131° for PEACl-modified CFM film versus 0.163° for pristine CFM film), which is beneficial to decrease the structural disorders in grain interiors and/or at GBs.[14] Specifically, the intensity enhancement of the characteristic (100) peak suggests the grains of the PEACl-modified film are more oriented, possibly by influencing the perovskite-substrate interfacial energy and the surface energy of perovskite. We propose that introduction of PEACl additives is able to reinforce the substrate/perovskite interaction and facilitate heterogeneous nucleation, which reduces the interfacial energy via improving the contact affinity between perovskite and underlying poly(triaryl amine) (PTAA) layer.[15] Specifically, the $-NH_3^+$ of PEA^+ coordinates with perovskite and the phenyl group interacts with PTAA, an aromatic rich polymer, through π–π interactions. Effectively reducing the interfacial energy at substrate/perovskite interface using PEA^+ as a linker promotes the formation of (100)-oriented nuclei, and results in the growth of grains with (100) orientation. In addition, the

ADVANCED
SCIENCE NEWS
www.advancedsciencenews.com

ADVANCED
MATERIALS
www.advmat.de

PEA+ molecules could interact with the undercoordinated ions in perovskite through electrostatic force. The compensation of charge imbalance at the surface of nuclei with (100) orientation reduces the surface energy to stabilize (100) nuclei.[16–18]

There was no noticeable shift of XRD peaks toward lower angles, indicating no significant unit cell expansion in the perovskite lattice or incorporation of PEACl into the perovskite crystal structure.[4] Notably, addition of 6.7 mol% PEACl resulted in the formation of a 2D/3D mixed perovskite (Figure S2, Supporting Information), which in some cases would inhibit charge transport.[9,19] Compared to the pristine CFM film, the phase-pure CFM-PEACl film exhibited improved absorption over all wavelength regions (Figure S3, Supporting Information), which can be ascribed to enhanced phase purity and improved crystallinity. In addition, the absorption onset was barely changed, suggesting the bandgap was maintained upon addition of a small amount (0.83 mol%) of PEACl.

PEACl consists of a PEA+ cation and Cl anion. Cl anions have been broadly shown to enhance crystal growth and crystallization of perovskite, while they might evaporate during annealing stage.[12,20] We previously demonstrated that amines could stay within perovskite films even after annealing at relatively high temperatures owing to a strong chemical interaction between the amine groups and perovskites.[4] Fourier transform infrared (FTIR) spectra in Figure S4, Supporting Information, indicate the PEA+ cation still presented within the bladed CFM perovskite films after thermal annealing at 100 °C for 10 min, as is evident by observable characteristic spectral features, for example, aromatic C−H bending at ≈680–860 cm^{-1}, aromatic C=C stretch at ≈1500–1440 cm^{-1}, and aromatic C−H stretch at 3000–3100 cm^{-1}. Due to the larger molecular size of PEA+, it is unfavorable to occupy interstitial sites within the perovskite structure. PEA+ would instead prefer to either occupy A-site vacancies at perovskite grain surfaces or passivate crystallographic defects at the perovskite GBs by forming ionic interactions with under-coordinated I− ions, as schematically illustrated in Figure 1c. An X-ray photoelectron spectroscopy study revealed that the I 3d^5 signal peak shifted to a higher binding energy after PEACl modification (Figure S5, Supporting Information), suggesting the possibility of reduced electronic cloud density surrounding the iodine atom, thus indicating potential interaction via ionic bonding between PEA+ cations and under-coordinated I− ions for passivating negative charged defects.[21,22] The interaction between the ammonium group (−NH$_3^+$) of PEA+ and the perovskite surface or GBs leaves the bulky hydrophobic aromatic ring exposed, which enhances moisture tolerance of the CFM perovskite films. More importantly, we hypothesize that PEA+ cation is able to reduce the free energy of the α-phase FA-alloyed perovskite and ultimately enable phase stabilization by two mechanisms: 1) compensating charge imbalance at surfaces and grain boundaries; and 2) inducing a small biaxial strain. On one hand, the compensation of charge imbalance by PEA+ cation bonding with undercoordinated I− or at A-site vacancies will lower the surface energy and lower the free energy of the resulting α-phase perovskite. On the other hand, the PEA+ molecules that decorate the surface and grain boundaries of the perovskite film may be able to induce a small biaxial strain through π–π interactions between neighboring molecules. Relative to the α-phase, the δ-phase is significantly destabilized by biaxial strain to reduce the driving force of the transformation from α- to δ-phase, ultimately stabilizing the α-phase.[17,18]

As shown in **Figure 2**a, the bladed CFM film still has a rough surface and some big gaps between GBs. The grain sizes of the control CFM film were 100–200 nm with an averaged grain size of ≈150 nm (inset in Figure 2a). The FA-alloyed perovskites have a very fast crystallization, making it difficult to obtain uniform films compared to bladed MAPbI$_3$.[13] In contrast, the CFM-PEACl film (0.83 mol% PEACl) showed a relatively smoother surface and larger grains of 300–800 nm with larger averaged sizes of ≈500 nm (Figure 2b). The enlarged grain sizes and improved crystallinity for CFM-PEACl film can be ascribed to that the Cl ions lower the crystallization rate and induce the preferred grain orientation.[20,23–25] In addition, the smooth CFM-PEACl film enables conformal coating of the electron transport layer (ETL) and the cathode during device fabrication. Figure 2c presents the cross-sectional scanning electron microscopy (SEM) image of a completed PSC device. The PEACl-modified perovskite film shows a columnar character with the grains monolithic throughout the film. The completed PSC device is based on a layer-by-layer stacking of indium doped tin oxide (ITO) substrate, PTAA hole transport layer (HTL), perovskite layer, C$_{60}$/bathocuproine (BCP) ETL and copper (Cu) electrode (denoted as ITO/HTL/perovskite/ETL/Cu), with a p–i–n planar heterojunction architecture (Figure 2d). The current density–voltage (J–V) curves for the best-performing PSCs based on CFM perovskite films with or without PEACl modification are shown in Figure 2e. Specifically, the champion PCE for the CFM-PEACl device reached 22.0% (**Table 1**), which was significantly higher than the pristine CFM counterpart (18.2%). The enhanced device performance with PEACl modification was mainly due to the enhanced V_{oc} and fill factor (FF). As is clearly observed in the external quantum efficiency (EQE) measurement in Figure 2f, the optical bandgap of both CFM and CFM-PEACl perovskite films was determined to be ≈1.51 eV based on the onset (821 nm) of the EQE spectra. Compared with the control CFM device, the V_{oc} of the CFM-PEACl device increased significantly by 60 mV, which yields a very small V_{oc} deficit of 0.33 V.

A high short-circuit current density (J_{sc}) larger than 23 mA cm^{-2} has been achieved for the CFM-PEACl based PSCs. The calculated J_{sc} values from the EQE spectra are 22.9 and 22.3 mA cm^{-2} for the CFM-PEACl and CFM devices, respectively, agreeing well with the J–V results with <3% discrepancy. The hysteresis in the best-performing CFM-PEACl device was negligible, with only a 0.9% absolute PCE discrepancy between the forward and reverse scans (Figure 2g; Table S3, Supporting Information). The champion device was held at a maximum power point of 0.98 V and the J_{sc} was steadied within seconds, giving a stabilized power output of 21.8% under AM 1.5 G illumination (Figure 2h). This high stabilized PCE outperforms the previously demonstrated MAPbI$_3$-based PSCs owing to the beneficially higher component of FA cations.[4] The PCE histogram of CFM and CFM-PEACl based PSCs were constructed from data collected from a batch of 30 devices for each condition (Figure 2i). The CFM-PEACl devices consistently showed higher PCEs, with better reproducibility than the CFM-based counterparts. Exceptionally, in this work, more than 93% of
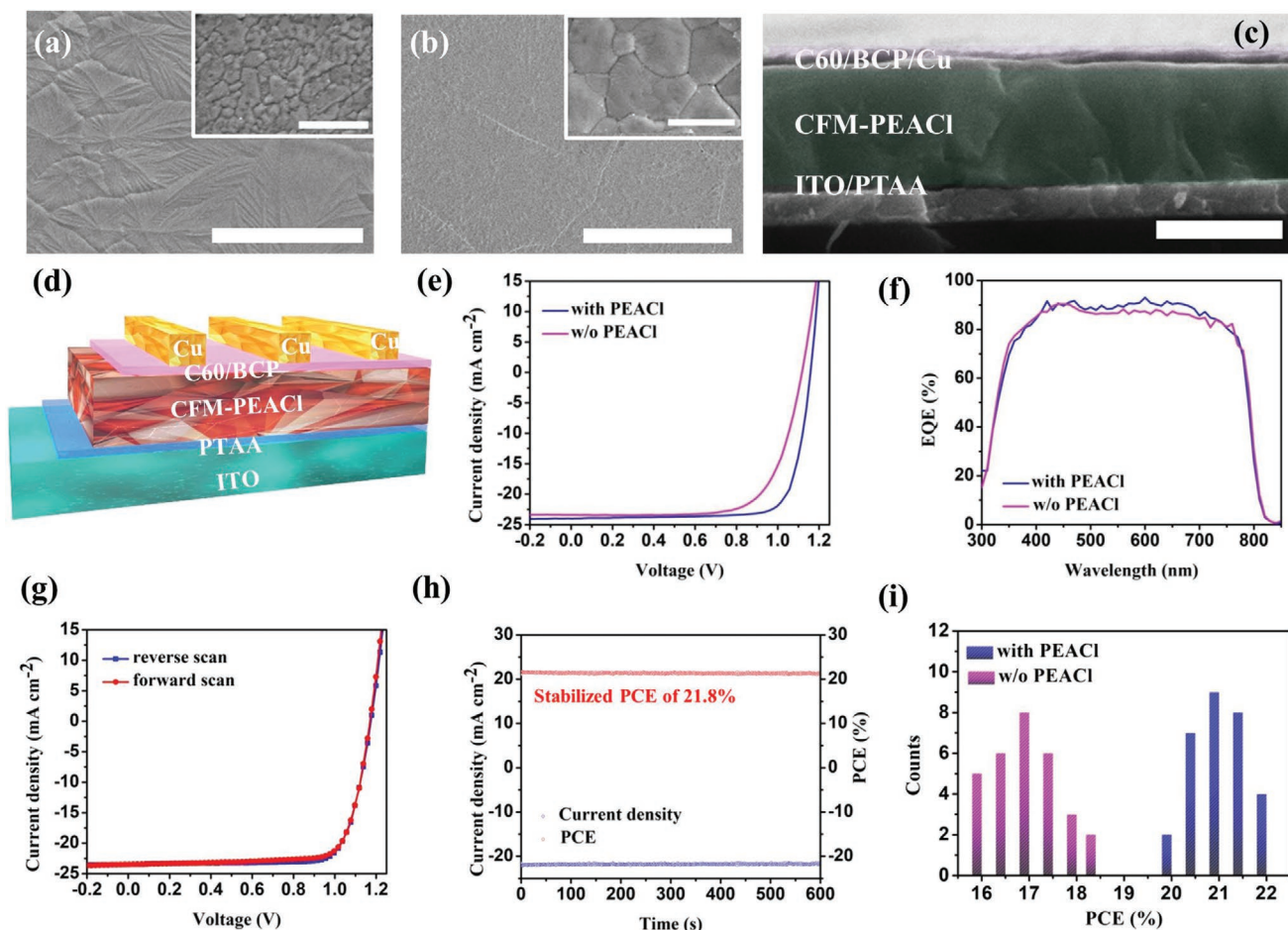
Figure 2. a,b) Surface SEM images of CFM (a) and CFM-PEACl (b) (the scale bars in (a) and (b) are 100 μm and 500 nm in the insets). c) Cross-sectional SEM image of a completed PSC device (the scale bar is 500 nm). d) Schematic illustration of an inverted p–i–n device structure. e) J–V curves and f) EQE spectra of PSCs based on CFM perovskite in the absence or presence of PEACl additive. g) J–V curves of the champion PSC with PEACl passivation measured under forward and reverse scanning directions. h) Stabilized current density and PCE at the maximum power point (0.98 V) of the champion device (0.08 cm^2) based on the CFM-PEACl thin film. i) PCE histogram of the PSCs based on CFM and CFM-PEACl films.

CFM-PEACl devices had PCEs above 20.5%, while only 36% of the control CFM devices had efficiencies over 17% under 1 sun illumination. This result highlights the effectiveness of PEACl modification on improving film compactness and uniformity, and thus improving the reproducibility of device performances.

Steady-state and time-resolved photoluminescence (PL) measurements were carried out to identify the passivation effect of PEACl molecules on perovskite films. In general, spontaneous radiative recombination via trap states normally leads to a red-shifted emission, and passivation of these trap states can blue-shift the PL emission peak.[26–28] As shown in **Figure 3**a

Table 1. Photovoltaic parameters of PSCs based on CFM perovskite (with a bandgap of 1.51 eV) with or without PEACl modification under 1 sun illumination (AM 1.5 G, 100 mW cm^{-2}).

PSCs	J_{sc} [mA cm^{-2}]	V_{oc} [V]	η [%]	Average η [%]	FF [%]	V_{oc} deficit [V]
CFM	23.0	1.12	18.2	16.88 ± 1.32	70.8	0.39
CFM-PEACl	23.6	1.18	22.0	21.25 ± 0.75	79.0	0.33

Data for average PCE (η) were calculated from at least 30 devices.

and Table S4, Supporting Information, the steady-state PL intensity was enhanced, accompanied by a ≈3 nm blue-shift upon addition of 0.83 mol% PEACl, irrespective of whether the PL was emitted from the top or bottom of the perovskite film. This indicates an efficient defect passivation effect induced by PEACl. The spatial distribution of PEACl molecules in the perovskite films is largely dependent on the fabrication process, which would consequently affect the PL peak positions and intensities. Upon PEACl addition, the top surface exhibited a nearly one-fold enhancement of PL intensity, while only a 40% increase of PL intensity was observed for bottom side of the film, suggesting that the top surface was more effectively passivated by PEACl. Though the PEACl is uniformly added into perovskite precursor, due to the large molecular size of the PEA$^+$, it is less likely to be incorporated into the crystal structure and ultimately be excluded to the grain boundaries and the surface of perovskite films, where it is then capable of passivating surface defects. Time-resolved photoluminescence (TRPL) lifetimes were measured for CFM perovskite films with and without PEACl modification, and the profiles were fitted with bi-exponential decays. The relatively fast decay component (τ_1)

**ADVANCED
SCIENCE NEWS**

www.advancedsciencenews.com

**ADVANCED
MATERIALS**

www.advmat.de
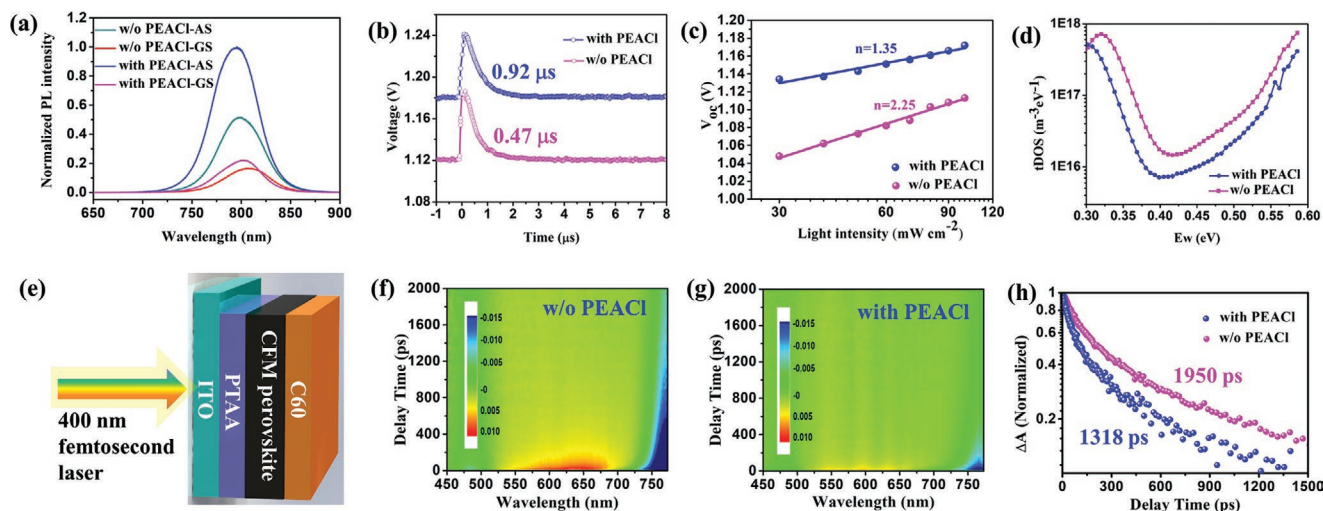
Figure 3. Photoluminescence, carrier recombination lifetime, ideal factor, trap densities, and transient absorption. a) PL spectra of perovskite films with or without PEACl emitted from either the air side (AS, top) or glass side (GS, bottom). b) Carrier recombination lifetime measured by TPV. c) V_{oc} dependence as a function of light intensities and d) trap density of states (tDOS) obtained from TAS measurement of perovskite devices with or without PEACl passivation. e) Schematic of the layer-stacking structure for TA measurement, where a 400 nm pump pulse generated by a fs laser was used to probe the TA signal. f,g) Contour plot TA spectra and h) dynamic TA decay probed at the GSB peak for CFM perovskite films with or without PEACl modification.

was assigned to the charge trapping process, while the much slower decay components (τ_2) were assigned to de-trapping or carrier recombination processes.[29] Upon PEACl passivation, the TRPL decay is largely dominated by the long decay process in the CFM-PEACl film and τ_2 was significantly elongated from 0.69 to 1.58 µs (Figure S6 and Table S5, Supporting Information). These results implied that the carrier recombination in PEACl-modified perovskite films was largely suppressed, suggesting reduced trap densities. The device was then irradiated under AM 1.5 G illumination and a small transient photovoltaic signal was triggered by a laser pulse (337 nm, 4 ns) to measure the transient photovoltage (TPV) decay.[30] The carrier recombination lifetime increased from 0.47 µs in the CFM device to 0.92 µs for the PEACl-modified device (Figure 3b). We also conducted electrochemical impedance spectroscopy (EIS) characterization and analysis to understand the charge recombination dynamics within the devices (Figure S7a,b, Supporting Information). Accordingly, the recombination resistance (R_{rec}) and carrier lifetime (τ_e) of the PSCs were calculated by fitting the EIS spectra with an equivalent circuit model (Figure S7e, Supporting Information). The PSC modified with PEACl showed both larger recombination resistance and longer carrier lifetime (Figure S7c,d and Table S6, Supporting Information) than the control device without PEACl modification. These results suggest the passivation by PEACl suppresses charge recombination, which enhanced V_{oc} of the CFM-PEACl device.

The light-intensity dependent V_{oc} was also measured to provide more information on charge recombination process in PSCs. By fitting the results to the equation, $n = kT/q\Delta V_{oc}/\Delta\ln J_L$ (where k, T, q, and J_L are the Boltzmann constant, absolute temperature, elementary charge, and photogenerated current density, respectively), the diode ideal factor (n) can be obtained.[31] In general, n can vary between 1 and 3 for PSCs depending on trap-assisted recombination.[32,33] The CFM-PEACl device exhibited a larger V_{oc} than the control CFM device under all

light intensities. The n decreased from 2.25 for the control CFM device to 1.35 for the CFM-PEACl device (Figure 3c), which is much closer to that of an ideal diode, indicating the nonradiative recombination process was effectively suppressed by PEACl passivation.[34] The prolonged carrier lifetime and suppressed nonradiative recombination of PSCs with PEACl passivation can be attributed to an effective reduction of trap densities within the perovskite films. Thermal admittance spectroscopy (TAS), a well-established characterization technique in thin-film photovoltaics,[35] was performed to quantify the trap density of states (tDOS) of the control and PEACl-modified devices. Figure 3d shows that the CFM-PEACl device had lower tDOS over the whole trap depth region compared to the pristine CFM counterpart. We inferred that surface defects/trap states at grain surfaces and/or GBs were effectively passivated upon PEACl modification, which resulted in reduced charge recombination loss, and thus higher V_{oc}, FF, and ultimately, a decent PCE for blade-coated PSCs.

It is reported that the photo-excited charge transfer process at interfaces within PSCs occurs on a timescale of picoseconds, which significantly affects charge extraction and collection.[36] We used femtosecond (fs) transient absorption (TA) spectroscopy to characterize the ultrafast carrier dynamic of the perovskite film, which is sandwiched between the PTAA HTL and C_{60} ETL contacts (Figure 3e). As shown in Figure 3f,g, the contour plots of the TA spectra for both CFM and CFM-PEACl samples exhibit a distinct ground-state bleaching (GSB) peak at ≈750 nm. The GSB peak intensity reflects the photoinduced carrier population in the conduction and valence bands of perovskite.[37,38] In contrast to the control CFM sample, a promptly fading signal in the contour plot for the CFM-PEACl sample suggested that photo-induced electrons and holes were more efficiently extracted out to the ETL and HTL. Accordingly, the decay kinetics of the GSB were analyzed, revealing a much faster decay for the sample with PEACl modification than that

**ADVANCED
SCIENCE NEWS**

www.advancedsciencenews.com

**ADVANCED
MATERIALS**

www.advmat.de
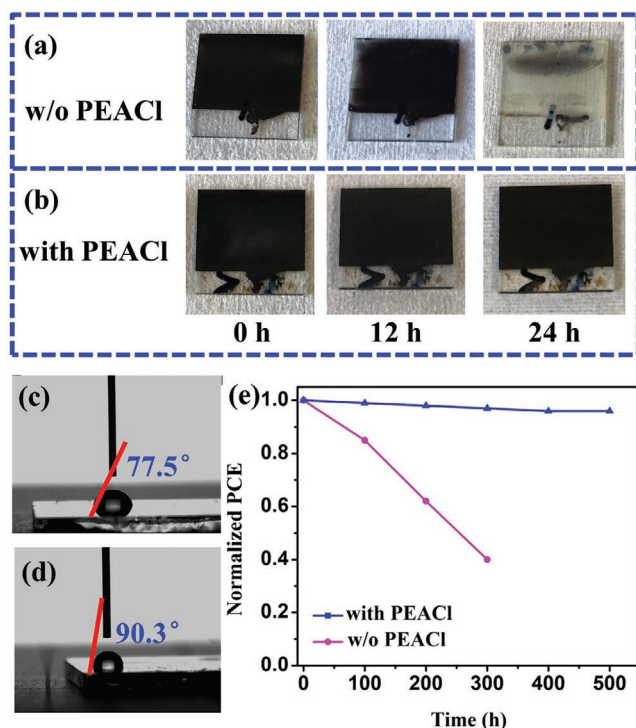
Figure 4. a,b) Photographs of CFM perovskite films modified with or without PEACl after prolonged exposure to 80 ± 5% RH environment for 24 h. c,d) Contact angle of a water droplet on the surface of a CFM perovskite film without (c) or with (d) PEACl modification. e) Operational stability of encapsulated PSCs based on CFM and CFM-PEACl films under continuous 1 sun illumination.

of the control CFM sample (i.e., 1318 ps vs 1950 ps, Figure 3h; Table S7, Supporting Information). This result verified the beneficial role of PEACl modification on accelerating charge extraction and collection from perovskite to the respective carrier transport layers, which could be ascribed to the improved quality of the CFM-PEACl perovskite film with enhanced phase purity, crystallinity, and reduced defect densities.[39,40]

The FA-alloyed perovskite is liable to undergo a phase transformation from cubic black-phase perovskite to yellow-phase nonperovskite under ambient conditions, especially in high relative humidity (RH).[8,41] To evaluate the effects of PEACl modification on phase stability, we traced the degradation of the perovskite films under RH of 80 ± 5%. **Figure 4**a,b shows photographs of perovskite films stored for different durations. The control CFM was almost completely bleached after 24 h owing to its transformation to the δ-phase (Figure 4a; Figure S8, Supporting Information), while no obvious change in color was observed for the CFM-PEACl film (Figure 4b), suggesting that PEACl addition enhanced phase stability in a high humidity environment. The defective surface and GBs of perovskite film are vulnerable to moisture invasion.[42] As aforementioned, the large, hydrophobic PEA$^+$ cation strongly bonds with the perovskite, and thus self-assembles a moisture-repelling barrier at the boundaries and surface of perovskite grains (Figure 1c). As shown in Figure 4c,d, the surface contact angle of water droplets increased from 77.5° on the CFM film to 90.3° on the PEACl-modified CFM film, which implied that possible

ingression pathways of moisture into the perovskite film were largely prohibited and decomposition of perovskite under atmospheric condition would be retarded. Besides the high initial PCE performance, the operational stability of PSCs under realistic conditions should be considered.[43] The stability of encapsulated PSCs based on CFM and CFM-PEACl films were compared under continuous 1 sun illumination. The CFM-PEACl device retained 96% of its initial PCE after 500 h, while the CFM device degraded to about 40% of its original PCE after 300 h (Figure 4e), indicating the significantly improved stability with the addition of PEACl. Only a very minor drop in photovoltaic parameters (i.e., J_{sc}, V_{oc}, FF, and PCE) has been recorded for the CFM-PEACl devices (Figure S9, Supporting Information), which can be attributed to an increase in temperature up to 60 °C during device operation.[44] Under operational conditions with abundant photogenerated charges and a built-in electric field, the degradation of device performance is normally caused by the presence of high concentrations of mobile charged or neutralized ions/defects that can lead to undesirable recombination loss.[45] In this work, the charged defects and/or undercoordinated ions at grain surfaces and/or GBs are effectively passivated by the addition of a robust passivation agent like PEACl. The enhanced phase purity of the CFM-PEACl film may also partially contribute to the enhanced operational stability, because the secondary, heterogeneous δ-phase nonperovskite can generate numerous active defect sites for charge recombination.

In summary, we have demonstrated the beneficial roles of organic halide molecules, particularly PEACl, in improving optoelectronic properties by improving the phase purity, reducing trap-state density, and facilitating charge collection. The PEACl modification strategy enabled us to demonstrate blade-coated devices based on FA-dominant perovskites with an impressive efficiency up to 22% and a good operational stability. We anticipate the chemical-modification via a combination of composition engineering and additive engineering is a promising strategy to stabilize perovskite with improved quality and optimal bandgap for prosperous optoelectronic applications.

Experimental Section

Materials: Unless stated otherwise, all materials and solvents were purchased from Sigma-Aldrich. Lead iodide (PbI$_2$, 99.999%) and cesium iodide (CsI) were purchased from Alfa Aesar. Formamidinium iodide (FAI) and methylammonium iodide (MAI) were purchased from GreatCell Solar.

Device Fabrication: The ITO glass substrates were cleaned ultrasonically in deionized water, acetone, and isopropyl alcohol baths for 30 min successively, followed by a UV–ozone (UVO) treatment for 15 min. A ≈20 nm thick PTAA layer was blade-coated onto the ITO glass according to previous report.[4] The perovskite layers were also fabricated via a blade-coating method.[4] The Cs$_{0.05}$FA$_{0.70}$MA$_{0.25}$PbI$_3$ perovskite ink (1.2 M) was prepared by dissolving PbI$_2$, FAI, MAI, and CsI in dimethylformamide (DMF). Before use, small amounts of additives, that is, methylammonium hypophosphite (0.15 wt%) and L-α-phosphatidylcholine (0.05 wt%), were added to achieve uniform perovskite film coating with good surface coverage.[3,46] A series of organic halide salts, that is, PEACl, PEABr, and PEAI were dissolved in DMF separately, then added to the as-prepared perovskite ink at an optimized concentration of 0.83 mol%. 5–10 µL of perovskite ink

was used for each blade-coating on a pre-heated 1.5 cm × 1.5 cm ITO substrate, and the film applicator was swiped linearly at a speed of 7.5 mm s^{-1}. After coating, the perovskite films were annealed at 100 °C for 10 min. Finally, 25 nm of C$_{60}$ (Nano-C), 8 nm of BCP, and 80 nm of Cu electrode were sequentially deposited by thermal evaporation to assemble a complete PSC device.

Device Characterization: SEM images were investigated by a Quanta 200 FEG environmental SEM. XRD patterns were recorded with a Bruker D8 Discover Diffractometer with Cu Kα radiation (1.5406 Å). The FTIR spectra (4000–500 cm^{-1}) were recorded on a PerkinElmer FTIR spectrometer with powders scratched from several pieces of samples. The *J–V* measurement of the devices (voltage scanning rate 0.1 V s^{-1}) and the steady photocurrent under maximum power output bias (0.98 V) were recorded with a Keithley 2400 source-meter under simulated AM 1.5 G irradiation produced by a xenon lamp based solar simulator (Oriel Sol3A, Class AAA Solar Simulator). The light intensity was calibrated by a silicon reference cell equipped with a Schott visible color KG5 glass filter (Newport 91 150 V). A nonreflective shadow mask was used to define a 0.08 cm^2 active area of the PSCs. EQE spectra were measured by a Newport QE measurement kit by focusing a monochromatic light beam with wavelength from 300 to 900 nm onto the devices. Photoluminescence (PL) spectrum was measured with a Horiba iHR320 Imaging Spectrometer at room temperature. A 532 nm green laser (Laserglow Technologies) with an intensity of 100 mW cm^{-2} was used as the excitation source. TRPL was obtained using a DeltaPro TCSPC Filter Fluorometer with a pulsed laser source at 406 nm (Horiba NanoLED 402-LH; pulse width below 200 ps, 20 pJ per pulse, ≈1 mm^2 spot size), and the signal was recorded using time-correlated single photon counting (TCSPC). The tDOS measurement was performed by using an Agilent E4980A precision LCR meter. The DC bias was fixed at 0 V and the amplitude of the AC bias was 20 mV. The scanning range of the AC frequency was 0.02–2000 kHz. The tDOS ($N_T (E_\omega)$) is calculated by using the equation: $N_T (E_\omega) = -\frac{1}{qkT}\frac{\omega dC}{d\omega}\frac{V_{bi}}{W}$, where W and V_{bi} are the depletion width and build-in potential, respectively, which were derived from the Mott–Schottky analysis of the *C–V* measurement. q, k, T, ω, and C are elementary charge, Boltzmann's constant, temperature, angular frequency, and specific capacitance, respectively. The demarcation energy $E_\omega = kT \ln\left(\frac{\omega_0}{\omega}\right)$ (where ω_0 is the attempt-to-escape angular frequency that equals to $2\pi\nu_0 T^2$ (ν_0 is the temperature-independent attempt-to-escape frequency)) is derived from the temperature-dependent *C–f* measurements which were carried out in a Lake Shore Cryotronics probe stage with a Lake Shore Cryotronics temperature controller model 336. TPV decay was measured under one sun illumination and recorded by a 1 GHz Agilent digital oscilloscope. The EIS measurements were carried out by using an electrochemical workstation (Zahner Zennium) with the frequency range from 1 Hz to 1 MHz under dark and different applied biases from −0.9 to −1.1 V. TA measurement was conducted by using a regeneratively amplified Ti:sapphire laser source (Coherent Legend, 800 nm, 150 fs, 5 mJ per pulse, and 1 kHz repetition rate) and Helios spectrometers (Ultrafast Systems LLC). A portion of the 800 nm output (75%) pulse was frequency doubled in a BaB$_2$O$_4$ (BBO) crystal, which could generate 400 nm pump light; the remaining portion of the output was concentrated into a sapphire window to produce a white light continuum (420–780 nm) probe light. The 400 nm pump beam was generated as part of the 800 nm output pulse from the amplifier and its power was adjusted by using a range of neutral-density filters. The pump beam was focused at the sample with a beam waist of about ≈360 mm and the power intensity was fixed at 14 μJ cm^{-2} in this experiment. With the aid of a mechanical chopper, the pump repetition frequency was synchronized to 500 Hz. The probe and reference beams could be split from the white light continuum and sent into a fiber optics-coupled multichannel spectrometer by using complementary metal-oxide-semiconductor sensors with a frequency of 1 kHz.

Supporting Information

Supporting Information is available from the Wiley Online Library or from the author.

Conflict of Interest

The authors declare no conflict of interest.

[1] N. S. Lewis, *Science* **2007**, *315*, 798.

[2] H. Eggers, F. Schackmar, T. Abzieher, Q. Sun, U. Lemmer, Y. Vaynzof, B. S. Richards, G. Hernandez-Sosa, U. W. Paetzold, *Adv. Energy Mater.* **2019**, *10*, 1903184.

[3] Y. Deng, X. Zheng, Y. Bai, Q. Wang, J. Zhao, J. Huang, *Nat. Energy* **2018**, *3*, 560.

[4] W.-Q. Wu, Z. Yang, P. N. Rudd, Y. Shao, X. Dai, H. Wei, J. Zhao, Y. Fang, Q. Wang, Y. Liu, Y. Deng, X. Xiao, Y. Feng, J. Huang, *Sci. Adv.* **2019**, *5*, eaav8925.

[5] S.-H. Turren-Cruz, A. Hagfeldt, M. Saliba, *Science* **2018**, *362*, 449.

[6] N. J. Jeon, H. Na, E. H. Jung, T.-Y. Yang, Y. G. Lee, G. Kim, H.-W. Shin, S. Il Seok, J. Lee, J. Seo, *Nat. Energy* **2018**, *3*, 682.

[7] W. S. Yang, B.-W. Park, E. H. Jung, N. J. Jeon, Y. C. Kim, D. U. Lee, S. S. Shin, J. Seo, E. K. Kim, J. H. Noh, S. I. Seok, *Science* **2017**, *356*, 1376.

[8] N. J. Jeon, J. H. Noh, W. S. Yang, Y. C. Kim, S. Ryu, J. Seo, S. I. Seok, *Nature* **2015**, *517*, 476.

[9] J.-W. Lee, Z. Dai, T.-H. Han, C. Choi, S.-Y. Chang, S.-J. Lee, N. De Marco, H. Zhao, P. Sun, Y. Huang, Y. Yang, *Nat. Commun.* **2018**, *9*, 3021.

[10] Z. Wang, Q. Lin, F. P. Chmiel, N. Sakai, L. M. Herz, H. J. Snaith, *Nat. Energy* **2017**, *2*, 17135.

[11] F. Wang, W. Geng, Y. Zhou, H.-H. Fang, C.-J. Tong, M. A. Loi, L.-M. Liu, N. Zhao, *Adv. Mater.* **2016**, *28*, 9986.

[12] S. Tang, Y. Deng, X. Zheng, Y. Bai, Y. Fang, Q. Dong, H. Wei, J. Huang, *Adv. Energy Mater.* **2017**, *7*, 1700302.

[13] Y. Deng, Q. Dong, C. Bi, Y. Yuan, J. Huang, *Adv. Energy Mater.* **2016**, *6*, 1600372.

[14] D.-Y. Son, J.-W. Lee, Y. J. Choi, I.-H. Jang, S. Lee, P. J. Yoo, H. Shin, N. Ahn, M. Choi, D. Kim, N.-G. Park, *Nat. Energy* **2016**, *1*, 16081.

[15] D. Chatterjee, R. Akash, K. Kamalnath, R. Ahmad, A. K. Singh, N. Ravishankar, *J. Phys. Chem. C* **2017**, *121*, 10027.

[16] B. J. Foley, J. Girard, B. A. Sorenson, A. Z. Chen, J. Scott Niezgoda, M. R. Alpert, A. F. Harper, D.-M. Smilgies, P. Clancy, W. A. Saidi, J. J. Choi, *J. Mater. Chem. A* **2017**, *5*, 113.

[17] G. P. Nagabhushana, R. Shivaramaiah, A. Navrotsky, *Proc. Natl. Acad. Sci. USA* **2016**, *113*, 7717.

[18] J. A. Steele, H. Jin, I. Dovgaliuk, R. F. Berger, T. Braeckevelt, H. Yuan, C. Martin, E. Solano, K. Lejaeghere, S. M. Rogge, *Science* **2019**, *365*, 679.

[19] H. Zheng, G. Liu, L. Zhu, J. Ye, X. Zhang, A. Alsaedi, T. Hayat, X. Pan, S. Dai, *Adv. Energy Mater.* **2018**, *8*, 1800051.

[20] D. Zhao, C. Chen, C. Wang, M. M. Junda, Z. Song, C. R. Grice, Y. Yu, C. Li, B. Subedi, N. J. Podraza, X. Zhao, G. Fang, R.-G. Xiong, K. Zhu, Y. Yan, *Nat. Energy* **2018**, *3*, 1093.

[21] J.-F. Liao, W.-Q. Wu, J.-X. Zhong, Y. Jiang, L. Wang, D.-B. Kuang, *J. Mater. Chem. A* **2019**, *7*, 9025.

[22] W.-Q. Wu, P. N. Rudd, Z. Ni, C. H. Van Brackle, H. Wei, Q. Wang, B. R. Ecker, Y. Gao, J. Huang, *J. Am. Chem. Soc.* **2020**, *142*, 3989.

[23] J.-F. Liao, W.-Q. Wu, Y. Jiang, J.-X. Zhong, L. Wang, D.-B. Kuang, *Chem. Soc. Rev.* **2020**, *49*, 354.

[24] J.-X. Zhong, W.-Q. Wu, J.-F. Liao, W. Feng, Y. Jiang, L. Wang, D.-B. Kuang, *Adv. Energy Mater.* **2020**, *10*, 1902256.

[25] Q. Jiang, Y. Zhao, X. Zhang, X. Yang, Y. Chen, Z. Chu, Q. Ye, X. Li, Z. Yin, J. You, *Nat. Photonics* **2019**, *13*, 460.

[26] W.-Q. Wu, Q. Wang, Y. Fang, Y. Shao, S. Tang, Y. Deng, H. Lu, Y. Liu, T. Li, Z. Yang, A. Gruverman, J. Huang, *Nat. Commun.* **2018**, *9*, 1625.

[27] S. Yang, J. Dai, Z. Yu, Y. Shao, Y. Zhou, X. Xiao, X. C. Zeng, J. Huang, *J. Am. Chem. Soc.* **2019**, *141*, 5781.

[28] Y. Zhao, H. Tan, H. Yuan, Z. Yang, J. Z. Fan, J. Kim, O. Voznyy, X. Gong, L. N. Quan, C. S. Tan, J. Hofkens, D. Yu, Q. Zhao, E. H. Sargent, *Nat. Commun.* **2018**, *9*, 1607.

[29] M. Maiberg, T. Hölscher, S. Zahedi-Azad, R. Scheer, *J. Appl. Phys.* **2015**, *118*, 105701.

[30] X. Zheng, B. Chen, J. Dai, Y. Fang, Y. Bai, Y. Lin, H. Wei, X. C. Zeng, J. Huang, *Nat. Energy* **2017**, *2*, 17102.

[31] M. Bernechea, N. C. Miller, G. Xercavins, D. So, A. Stavrinadis, G. Konstantatos, *Nat. Photonics* **2016**, *10*, 521.

[32] F. Chengbin, L. Bo, Z. Rong, F. Haoyu, T. Jianjun, C. Guozhong, *Adv. Energy Mater.* **2017**, *7*, 1602017.

[33] S. Trilok, M. Tsutomu, *Adv. Energy Mater.* **2018**, *8*, 1700677.

[34] M. Stolterfoht, C. M. Wolff, Y. Amir, A. Paulke, L. Perdigon-Toro, P. Caprioglio, D. Neher, *Energy Environ. Sci.* **2017**, *10*, 1530.

[35] Y. Shao, Z. Xiao, C. Bi, Y. Yuan, J. Huang, *Nat. Commun.* **2014**, *5*, 5784.

[36] J. Lu, X. Lin, X. Jiao, T. Gengenbach, A. D. Scully, L. Jiang, B. Tan, J. Sun, B. Li, N. Pai, U. Bach, A. N. Simonov, Y.-B. Cheng, *Energy Environ. Sci.* **2018**, *11*, 1880.

[37] Z. Zhu, J. Ma, Z. Wang, C. Mu, Z. Fan, L. Du, Y. Bai, L. Fan, H. Yan, D. L. Phillips, S. Yang, *J. Am. Chem. Soc.* **2014**, *136*, 3760.

[38] J. P. C. Baena, L. Steier, W. Tress, M. Saliba, S. Neutzner, T. Matsui, F. Giordano, T. J. Jacobsson, A. R. S. Kandada, S. M. Zakeeruddin, A. Petrozza, A. Abate, M. K. Nazeeruddin, M. Grätzel, A. Hagfeldt, *Energy Environ. Sci.* **2015**, *8*, 2928.

[39] M. Zhang, S. Dai, S. Chandrabose, K. Chen, K. Liu, M. Qin, X. Lu, J. M. Hodgkiss, H. Zhou, X. Zhan, *J. Am. Chem. Soc.* **2018**, *140*, 14938.

[40] W.-Q. Wu, D. Chen, W. A. McMaster, Y.-B. Cheng, R. A. Caruso, *ACS Appl. Mater. Interfaces* **2017**, *9*, 31959.

[41] J.-W. Lee, D.-H. Kim, H.-S. Kim, S.-W. Seo, S. M. Cho, N.-G. Park, *Adv. Energy Mater.* **2015**, *5*, 1501310.

[42] Q. Wang, B. Chen, Y. Liu, Y. Deng, Y. Bai, Q. Dong, J. Huang, *Energy Environ. Sci.* **2017**, *10*, 516.

[43] Y. Rong, Y. Hu, A. Mei, H. Tan, M. I. Saidaminov, S. I. Seok, M. D. McGehee, E. H. Sargent, H. Han, *Science* **2018**, *361*, eaat8235.

[44] J. A. Schwenzer, L. Rakocevic, R. Gehlhaar, T. Abzieher, S. Gharibzadeh, S. Moghadamzadeh, A. Quintilla, B. S. Richards, U. Lemmer, U. W. Paetzold, *ACS Appl. Mater. Interfaces* **2018**, *10*, 16390.

[45] N. Ahn, K. Kwak, M. S. Jang, H. Yoon, B. Y. Lee, J.-K. Lee, P. V. Pikhitsa, J. Byun, M. Choi, *Nat. Commun.* **2016**, *7*, 13422.

[46] Z. Xiao, D. Wang, Q. Dong, Q. Wang, W. Wei, J. Dai, X. Zeng, J. Huang, *Energy Environ. Sci.* **2016**, *9*, 867.